

DSOcc: Leveraging Depth Awareness and Semantic Aid to Boost Camera-Based 3D Semantic Occupancy Prediction

Naiyu Fang^{1,4}, Zheyuan Zhou², Kang Wang², Ruibo Li¹, Lemiao Qiu², Shuyou Zhang²,
Zhe Wang³, Guosheng Lin^{1,4*}

¹NTU, S-Lab ²ZJU ³SenseTime Research ⁴NTU, CCDS

E-mail: naiyu.fang@ntu.edu.sg, gslin@ntu.edu.sg

Abstract

Camera-based 3D semantic occupancy prediction offers an efficient and cost-effective solution for perceiving surrounding scenes in autonomous driving. However, existing works rely on explicit occupancy state inference, leading to numerous incorrect feature assignments, and insufficient samples restrict the learning of occupancy class inference. To address these challenges, we propose leveraging **Depth** awareness and **Semantic** aid to boost camera-based 3D semantic **Occupancy** prediction (**DSOcc**). We jointly perform occupancy state and occupancy class inference, where soft occupancy confidence is calculated by non-learning method and multiplied with image features to make voxels aware of depth, enabling adaptive implicit occupancy state inference. Instead of enhancing feature learning, we directly utilize well-trained image semantic segmentation and fuse multiple frames with their occupancy probabilities to aid occupancy class inference, thereby enhancing robustness. Experimental results demonstrate that DSOcc achieves state-of-the-art performance on the SemanticKITTI dataset among camera-based methods.

1 Introduction

The perception of surrounding scenes serves as the foundational part of autonomous driving. Compared to the LiDAR-based scheme [41, 57], camera-based scheme [56, 7] has attracted significant attention due to the lower cost of devices. To achieve 3D perception, camera-based 3D semantic occupancy prediction [27, 54] represents the surrounding environment using a predefined voxel grid, where each voxel is annotated with a semantic label. This task marks a significant advancement towards cheap, clear, efficient scene understanding for autonomous driving.

Camera-based 3D semantic occupancy prediction extracts features from camera images and projects them onto

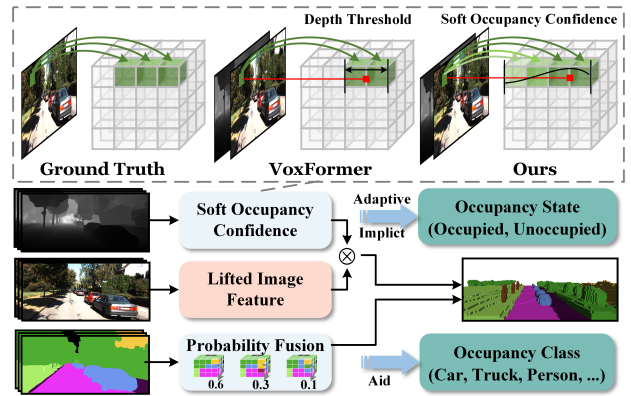


Figure 1: DSOcc computes a soft occupancy confidence from depth and embed it into image features, enabling adaptive implicit occupancy state inference. DSOcc fuses image semantic segmentation with occupancy probabilities to aid in occupancy class inference.

a voxel grid for prediction. This task requires consideration of two aspects: occupancy state and occupancy class. The occupancy state determines whether a voxel is occupied, while the occupancy class specifies which class a voxel belongs to. Typically, the model uses the projection matrix and depth information to predict the occupancy state, and then utilizes image features to predict the occupancy class.

For the occupancy state, two-stage methods [27, 38] and depth-query methods [19, 47] estimate a depth threshold to classify voxels as either occupied or unoccupied based on depth and voxel position. The issue arises when depth prediction or threshold estimation is inaccurate: since only occupied voxels are assigned features for subsequent classification, a truly occupied voxel may be misclassified as unoccupied, while its neighboring unoccupied voxel may incorrectly receive features. This phenomenon is common. Our analysis shows that in [27], nearly 40% of occupied voxels are misclassified as unoccupied (see Appendix A). To mitigate accumulated errors, it is crucial to reduce the heavy reliance on depth pre-

*Corresponding author. G. Lin. (e-mail: gslin@ntu.edu.sg)

diction or threshold estimation. For the occupancy class, the prediction accuracy relies on the mapping effect from image features to occupancy classes. To this end, previous methods have incorporated various modules to learn geometric features [50], instance cues [19], and semantic guidance [38]. However, a critical issue overlooked is that they are trained on limited datasets. For instance, SemanticKITTI [2] and SSCBenchKITTI-360 [28] contain only 3,834 and 8,487 training samples, respectively. Within this fact, effectively utilizing image features is akin to 'dancing in shackles', and the occupancy class prediction are constrained in this shackle.

To address these challenges, we propose depth awareness and semantic aid to boost 3D semantic occupancy prediction in the aspect of occupancy state and occupancy class. As illustrated in Fig. 1, We embed soft occupancy confidence into image feature to enable adaptive implicit occupancy state inference and integrate image semantic segmentation to enhance the robustness of occupancy class inference. Specifically, we perform occupancy state and occupancy class inference jointly, rather than treating them as independent subtasks. We directly calculate soft occupancy confidence by measuring the distance between voxel position and depth. The soft occupancy confidence is multiplied with the image features and assigned to the corresponding voxel. This prevents the loss of image features in false unoccupied voxel while enabling depth-aware image feature collection. We observe that 3D semantic occupancy prediction and image semantic segmentation share the same objective, while image semantic segmentation demonstrates better robustness when trained on large-scale datasets. Thus, we weight multi-frame semantic segmentation maps with occupancy probabilities to aid the occupancy class inference. Finally, we design a voxel fusion module to integrate the two voxel types for the final prediction. In summary, the main contributions of this work are summarized as follows:

- We propose calculating soft occupancy confidence in a non-learning method to embed depth into image features, enabling adaptive implicit occupancy state inference.
- We propose fusing multi-frame image semantic segmentation with occupancy probabilities to aid in occupancy class inference, thereby enhancing its robustness.
- Experiments demonstrate that our DSOcc achieves state-of-the-art results with 18.02 and 16.90 mIoU on the SemanticKITTI validation set and hidden test set, respectively.

2 Related Works

3D Semantic Occupancy Prediction. 3D semantic occupancy prediction originates from the semantic scene completion (SSC) task, first introduced in SSCNet [58]. SSC extracts images features, lifts them to a 3D representation, and then predicts voxels, each assigned a semantic label [33, 44, 22, 53, 32]. As autonomous driving tech-

nology advances [29, 9, 23], 3D semantic occupancy prediction has gained attention for providing clear and efficient representations. Among these, camera-based methods [5, 17, 54] are popular due to the cost-effectiveness of camera devices.

For camera-based 3D semantic occupancy prediction, dimensional transformation is a crucial component. MonoScene [5] firstly introduced a 2D-to-3D feature projection. OccFormer [54] leverages local and global transformers to perform projection along the horizontal plane. SurroundOcc [49] employed spatial projection to lift multi-scale features. COTR [37] introduced an explicit-implicit transformation for compact 3D representation. ViewFormer [24] proposed a learning-first view attention mechanism to aggregate multi-view features.

Following dimensional transformation, previous methods utilize depth information to resolve projection ambiguity during feature collection. Two-stage method [27, 38] learns an explicit occupancy status conditioned on depth and then collects features only for occupied voxels. The depth-query method [19, 47] uses depth as a query and interacts with features to embed depth information. Similar to LSS [40], methods in [55, 54] predict context and depth features from images and use the outer product to incorporate depth awareness. ViDAR [52] employs ray-casting renders to predict depth conditional probability and learns to multiply it with BEV features to embed depth information.

Inspired by [40, 52], DSOcc aims to calculate soft occupancy confidence based on depth and embed it into image features for occupancy status inference. This is achieved through direct calculation without requiring any learning module.

2D Image Representation. Besides image features, camera-based 3D semantic occupancy prediction also incorporates information from other inputs, such as depth, semantic segmentation, and instance segmentation. Depth estimation is a fundamental task in camera-based autonomous driving and can be categorized into relative depth [51, 13] and absolute depth [17, 10]. With monocular [25, 11] or stereo [3] images, absolute depth estimation provides the real distance between objects and the camera. Absolute depth information has been applied in camera-based 3D semantic occupancy prediction to resolve projection ambiguity in the frontal direction [27, 47], thereby helping to determine occupancy state.

Semantic segmentation [34] predicts a semantic label for each image pixel, while instance segmentation [26] distinguishes objects within a class based on it. Cityscapes [8], KITTI [1], and nuScenes [4] provide diverse driving scenes and conditions. By training on these datasets, many classic models, such as FCNs [34], and DeepLab [6], achieve robust and efficient segmentation for real-time application. Recently, universal segmentation models [21, 31] aim to improve scalability by training on mixed datasets.

Inspired by the above, DSOcc explores the use of depth and image semantic segmentation information to enhance camera-based 3D semantic occupancy prediction.

3 Methodology

3.1 Overview

The framework of DSOcc is illustrated in Fig. 2. We aim to take the multi-frame camera images $\{\mathbf{I}_t, \mathbf{I}_{t-1}, \dots, \mathbf{I}_{t-n}\} \in \mathbb{R}^{h \times w}$ and camera parameters $\{\mathbf{K}, \mathbf{T}\}$ as inputs to predict the 3D semantic occupancy $\mathbf{Y}_t \in \{c_0, c_1, \dots, c_M\}^{H \times W \times Z}$ at the timestep t . Here, $n + 1$ is the frame number of camera images; h, w denotes the height and width of camera image; \mathbf{K}, \mathbf{T} denote the intrinsic and extrinsic matrix of camera; $\mathbf{T} = [\mathbf{R}|\mathbf{t}]$ is composed of rotation matrix \mathbf{R} and translation matrix \mathbf{t} ; H, W, Z are the length, width, height of voxel grid; M denotes the class number of 3D semantic occupancy. In a word, the mathematical formulation is $\mathbf{Y}_t = \Theta(\{\mathbf{I}_{t-i}\}_{i=0}^n, \mathbf{K}, \mathbf{T})$, where Θ is the proposed DSOcc.

DSOcc aims to enhance the inference capacity of the occupancy state (whether) and the occupancy class (which) in 3D semantic occupancy prediction. It utilizes a pre-trained image encoder to extract image features $\{\mathbf{F}_{t-i}\}_{i=0}^n$, and employs a well-trained depth predictor and semantic segmentation model to infer depth maps $\{\mathbf{D}_{t-i}\}_{i=0}^n$ and semantic segmentation map $\{\mathbf{S}_{t-i}\}_{i=0}^n$. To address the challenges of ambiguous spatial correspondences between voxels and images in occupancy state inference, we lift 2D image features into depth-aware image feature voxels for each frame and obtain $\{\mathbf{V}_{t-i}^I\}_{i=0}^n$ by computing a soft occupancy confidence and backward project image features into a dense voxel. To aid the occupancy class inference, we lift semantic segmentation maps to a semantic-aided voxel \mathbf{V}_t^S by integrating multi-frame one-hot representations with occupancy probabilities. Concurrently, we propose a novel voxel fusion module that fuses $\{\mathbf{V}_{t-i}^I\}_{i=0}^n$ and \mathbf{V}_t^S to obtain \mathbf{V}_t^F by utilizing global interaction through deformable attention.

Depth Predictor. It estimates the absolute depth between objects and ego vehicle, conditioned on camera images and calibrations. Specifically, we leverage the well-trained MobileStereoNet [42], similar to previous method [19, 27]. This model is lightweight and well-suited for real-time applications.

Semantic Segmentation Model. It is pretrained on large-scale datasets, and exact class alignment with our task is not required. Specifically, we employ MSeg [21] and adapt its universal class classification to the specific class presets required for this task (see Appendix B).

3.2 Depth-Aware Image Feature Voxel

The voxels are projected into the image coordinates using camera calibration parameters, and the corresponding image features are collected. Similar to previous methods [5, 38], as illustrated in Fig. 3b, unoccupied voxels share the same projection position as neighboring occupied voxels in the absence of depth information. Consequently, these unoccupied voxels erroneously collect object-related information, leading to numerous incorrect occupancy state inferences. For previous methods [27, 47], they learn explicit occupancy states using depth information in a separate stage. Intrinsically, as illustrated in Fig. 3c, these methods employ a hard confidence truncation to provide a binary estimation for each voxel. According to our calculations, these methods misclassify nearly 40% of occupied voxels as unoccupied, resulting in these false unoccupied voxels failing to collect any features in the subsequent stages.

Therefore, in this section, we aim to learn a soft occupancy confidence conditioned on depth information and embed it into image features. This enables the model to adaptively infer occupancy states, identifying potential unoccupied voxels while allowing all voxels to learn image features from their projected positions.

As illustrated in Fig. 2, let P be the voxel center in the ego vehicle coordinate, and p is the corresponding projected point in the image coordinate. The projection process is described as follow:

$$p = \mathbf{K}(\mathbf{R}P + \mathbf{t}) \quad (1)$$

For the projected point $p = (x, y, z)$, its x, y values determine the pixel position, while its z value represents the distance between P and the camera. We compare z with its depth d from \mathbf{D} . Intuitively, when the real object is located in this voxel, z will be equal to d . Therefore, we calculate a soft occupancy confidence c to represent the distance between the voxel and the real object. The mathematical expression is given by:

$$c = \exp(-|z - d|) \quad (2)$$

The range of c is $(0, 1]$, and c will approach 1 when P is close to the real object at p , and vice versa.

Next, we aim embed this soft occupancy confidence into image features to form a depth-aware image feature voxel. For feature voxel establishment, previous methods [27, 19] use a learning-based approach to collect image features into the voxel. This requires additional computation and is prone to misalignment. In contrast, we explicitly establish the image feature voxel based on the projection relationship. We define a separate voxel for each frame and only illustrate the case at timestep t for convenience. For the soft occupancy confidence, we set $c = 0$ when the projected point p is outside the image dimension, and assign c at the corresponding position of P in

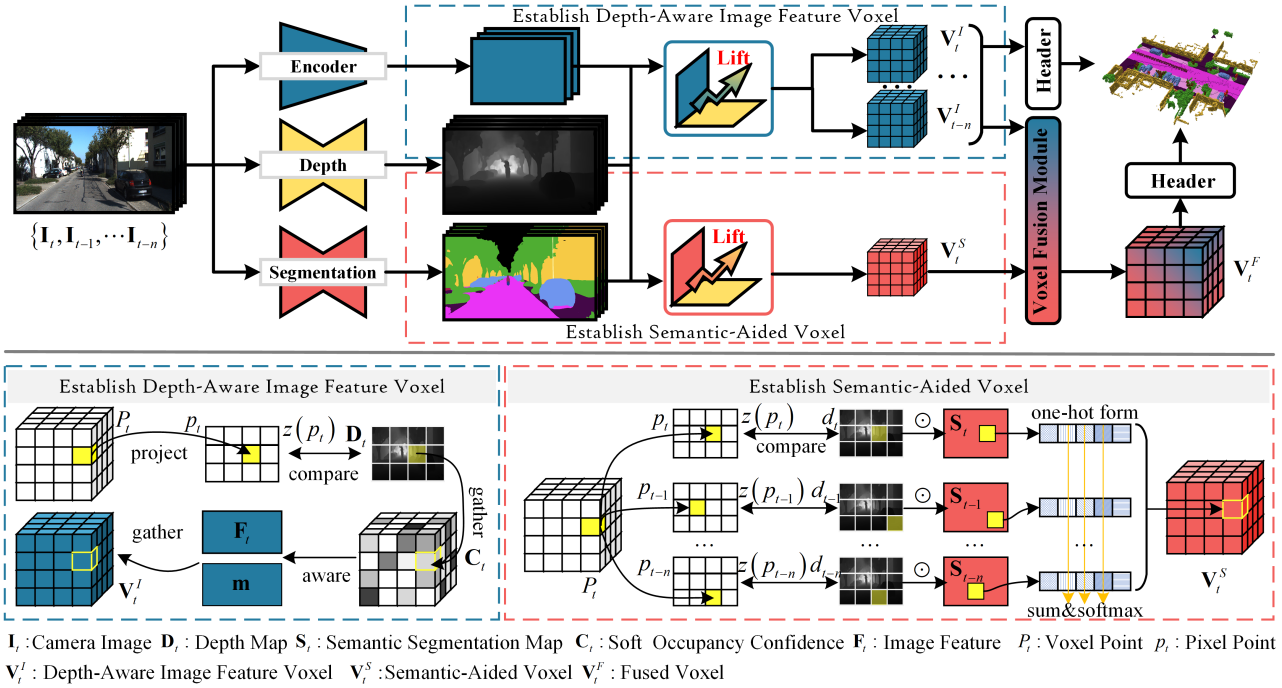


Figure 2: The framework of DSOcc. We embed soft occupancy confidence into image features for adaptive implicit occupancy state inference, fuses multi-frame semantic segmentation maps to aid occupancy class inference, and incorporates a voxel fusion module for final prediction.

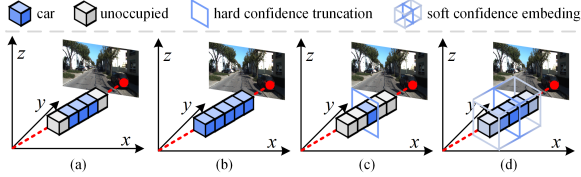


Figure 3: Occupancy state inference of different methods. (a) ground truth. (b) without depth information. (c) explicit occupancy state inference using hard confidence truncation. (d) our depth-aware approach: embedding a soft truncation.

voxel to obtain a depth-aware matrix C . For the image features, we devise a learnable matrix m as a marker for unoccupied voxels, and our feature voxel \tilde{F} is described as follow:

$$\tilde{F} = \begin{cases} F^\uparrow, p \in [0, w) \times [0, h) \\ m^\uparrow, p \notin [0, w) \times [0, h) \end{cases} \quad (3)$$

where \uparrow denotes collection operation. Lastly, we embed depth-aware matrix C into feature voxel \tilde{F} to obtain depth-aware image feature voxel V^I :

$$V^I = C \cdot \tilde{F} \quad (4)$$

With this depth-aware embedding, when the voxel is far from the real object, the image feature assigned to it is attenuated by the soft occupancy confidence. As the

distance increases, the image feature approaches zero, allowing the model to identify it as unoccupied.

3.3 Semantic-Aided Voxel

The core challenge in 3D semantic occupancy prediction is to identify the class of each voxel based on image features. However, due to limitations in model capacity and the dataset scale, prediction models face challenges such as class imbalance and poor class discrimination, as illustrated in Fig. 4c. In contrast, image semantic segmentation benefit from larger and more diverse datasets, achieving greater robustness. Fundamentally, both image semantic segmentation and 3D semantic occupancy prediction share the same objective, and the former class distribution closely resembles the latter ground truth, as illustrated in Fig. 4a and Fig. 4b. Therefore, we aim to use the former capacity in the latter task to aid occupancy class inference.

We establish a semantic-aided voxel to collect segmentation information from $\{S_{t-i}\}_{i=0}^n$ using the projection relationship defined as Equ. 1. As illustrated in Fig. 4d, the same voxel may collect different classes from different frames due to the projection shift between adjacent frames. Since the results are discrete, effectively utilizing segmentation information from multiple frames is a key challenge.

To address this, we aim to fuse segmentation with their

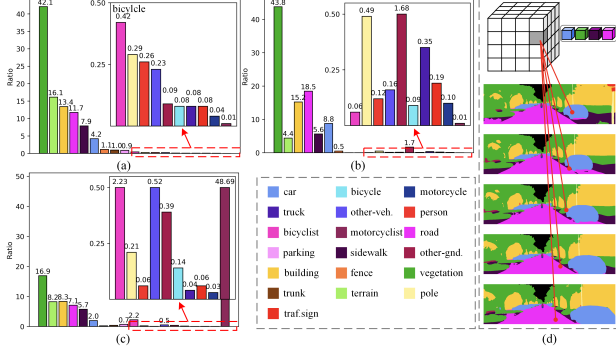


Figure 4: Class distribution on SemanticKITTI val dataset [2]. (a) ground truth. (b) semantic segmentation. (c) predictions conditioned on \mathbf{V}^I . (d) projection shift.

occupancy probabilities for sorting and weighted concatenation, enabling the subsequent module to adaptively extract useful segmentation despite projection shifts. Specifically, we transform $\{\mathbf{S}_{t-i}\}_{i=0}^n$ into the one-hot form, and utilize the soft occupancy confidence defined as Equ. 2 to determine the occupancy probabilities across frames. We then multiply the occupancy probabilities by one-hot form segmentation for each frame and sum results across all frames. In this way, when the distance between the voxel and the real object in one frame is smaller, the occupancy class of this voxel should more closely align with the segmentation of this frame. As illustrated in Fig. 2, we obtain the semantic-aided voxel \mathbf{V}_t^S at the timestep t as:

$$\mathbf{V}_t^S = \text{softmax} \left[\sum_{i=0}^n \left(\mathbf{C}_{t-i} \cdot \mathbf{S}_{t-i}^\uparrow \right) \right] \quad (5)$$

3.4 Voxel Fusion Module

In this section, we aim to fuse depth-aware image feature voxels $\{\mathbf{V}_{t-i}^I\}_{i=0}^n$ and semantic-aided voxel \mathbf{V}_t^S to obtain a fused voxel \mathbf{V}_t^F for final prediction. As illustrated in Fig. 4, initially, $\{\mathbf{V}_{t-i}^I\}_{i=0}^n$ are concatenated along the channel dimension and projected into $\tilde{\mathbf{V}}_t^I$ through a Conv3D layer, which maintains the original voxel size but reduces the channel number from nC to C . Similarly, \mathbf{V}_t^S is projected into $\tilde{\mathbf{V}}_t^S$, where the channel number is increased from M to C . Although the depth-aware image feature voxel and the semantic-aided voxel are aligned for each voxel, the model still needs to learn global spatial cues for prediction.

Since voxel interaction has cubic complexity, we employ the computation-efficient deformable attention (DA) [58] to learn global spatial cues. DA aggregates the feature \mathbf{F} into the query \mathbf{q} with several deformable reference points p . The mathematical expression is given by:

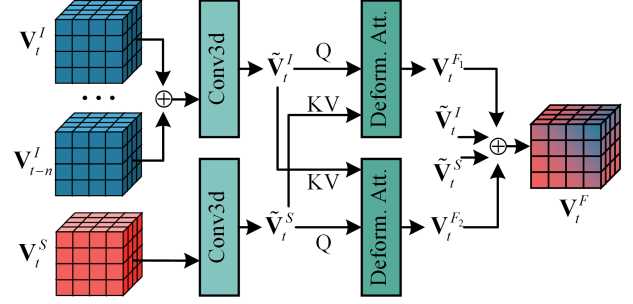


Figure 5: Voxel fusion module: The dual interaction mechanism aggregates segmentation and image feature information globally via deformable attention to obtain the fused voxel.

$$\text{DA}(\mathbf{q}, p, \mathbf{F}) = \sum_{s=1}^{N_s} \mathbf{A}_s \mathbf{W}_s \mathbf{F}(p + \Delta p_s) \quad (6)$$

where N_s denotes the number of sampling points, $\mathbf{A}_s \in [0, 1]$ denotes a learnable weight matrix conditioned on \mathbf{q} for the sampling point s , $\mathbf{W}_s \in \mathbb{R}^{C \times C}$ denotes the projection matrix for value transformation, and Δp_s is the predicted offset relative to p conditioned on \mathbf{q} .

Specifically, we propose a dual interaction mechanism for $\tilde{\mathbf{V}}_t^S$ and $\tilde{\mathbf{V}}_t^I$. $\tilde{\mathbf{V}}_t^I$ is utilized as a query to aggregate segmentation information from $\tilde{\mathbf{V}}_t^S$ with the voxel reference point P to obtain \mathbf{V}_t^{F1} . Conversely, $\tilde{\mathbf{V}}_t^S$ is utilized as query to aggregate image feature information from $\tilde{\mathbf{V}}_t^I$ to obtain \mathbf{V}_t^{F2} . This interaction process is described as:

$$\begin{cases} \mathbf{V}_t^{F1} = \text{DA} \left(\tilde{\mathbf{V}}_t^I, P, \tilde{\mathbf{V}}_t^S \right) \\ \mathbf{V}_t^{F2} = \text{DA} \left(\tilde{\mathbf{V}}_t^S, P, \tilde{\mathbf{V}}_t^I \right) \end{cases} \quad (7)$$

At the end of voxel fusion module, we concatenate $\tilde{\mathbf{V}}_t^I, \mathbf{V}_t^{F1}, \mathbf{V}_t^{F2}, \tilde{\mathbf{V}}_t^S$ along the channel dimension to obtain the fused voxel \mathbf{V}_t^F .

3.5 Losses

During the training phase, we use two headers consisting of Conv3D layers to predict \mathbf{Y}_t and \mathbf{Y}_{ti} conditioned on \mathbf{V}_t^F and $\tilde{\mathbf{V}}_t^I$ at the timestep t , respectively. The prediction of \mathbf{Y}_{ti} supervises the extraction and learning of image features. Similar to previous methods [19, 27, 38], we employ the standard semantic loss \mathcal{L}_{sem} and geometric loss \mathcal{L}_{geo} as defined in Monoscene [5] to supervise predictions $(\mathbf{Y}_t, \mathbf{Y}_{ti})$ at the semantic and geometric level, respectively. We also use the weighted cross-entropy loss \mathcal{L}_{ce} , where the weight is calculated from class frequency. The overall loss function is defined as:

$$\mathcal{L} = \sum_{x \in \{t, ti\}} (\mathcal{L}_{sem}(\mathbf{Y}_x, \hat{\mathbf{Y}}_t) + \mathcal{L}_{geo}(\mathbf{Y}_x, \hat{\mathbf{Y}}_t) + \mathcal{L}_{ce}(\mathbf{Y}_x, \hat{\mathbf{Y}}_t)) \quad (8)$$

where \hat{Y}_t denotes the ground truth for 3D semantic occupancy prediction. Additionally, there are no hyperparameters to balance the different losses and prediction branches, ensuring its scalability.

During the testing phase, we select Y_t as the final prediction, and the header for predicting Y_{ti} is no longer needed.

4 Experiment

4.1 Dataset

Dataset. We evaluate DSOcc on the SemanticKITTI [2] and SSCBenchKITTI-360 [28] datasets. Both datasets focus on a scene of $51.2m \times 51.2m \times 6.4m$, with a voxel size of $0.2m \times 0.2m \times 0.2m$. SemanticKITTI includes 20 class labels (19 semantics + 1 free), whereas SSCBenchKITTI-360 includes 19 class labels (18 semantics + 1 free).

Metric. Following SSC, we measure performance using intersection over union (IoU) and mean IoU (mIoU) over 19 classes. IoU reflects overall scene completion quality, while mIoU the quality of semantic segmentation for each class. We report mIoU as our primary metric.

4.2 Implementation Details

We crop images into size 1220×370 , and use ResNet50 [14] to extract its feature map. All experiments were conducted on 2 NVIDIA A6000 GPUs with a batch size of 1. The DA used in the voxel fusion module has 1 layer and 8 sampling points. We optimize DSOcc using the AdamW optimizer [35] with an initial learning rate of $2 \times e^{-4}$ and a weight decay of $1 \times e^{-4}$ for a total of 40 epochs. Following the method in [27, 46, 38, 47], we propose two versions of the DSOcc model: **DSOcc-T**, which takes the current and previous four frames as inputs, and **DSOcc-S**, which takes only the current frame as input.

4.3 Main Results

Qualitative Comparisons. We present the qualitative comparison results on the SemanticKITTI validation set, the SemanticKITTI hidden test set, and the SSCBenchKITTI-360 test set in Table 1, Table 2, and Table 3, respectively. For a more comprehensive evaluation, additional comparisons on Occ3D-NuScenes [45] are included in Appendix C.3. On the SemanticKITTI dataset, DSOcc-T achieves the highest mIoU of 18.02 (+2.14) and 16.90 (+0.17) on the validation and hidden test sets, respectively, outperforming 12 and 9 classes out of the total 19 classes. DSOcc-S also demonstrates state-of-the-art performance among S-version models, with mIoU scores of 14.59 (+0.04) and 14.96 (+0.95) on the validation and hidden test sets, respectively. On the SSCBench-KITTI-360 test set, DSOcc maintains competitive performance,

achieving 17.51 mIoU for S-version, demonstrating the robustness of our method.

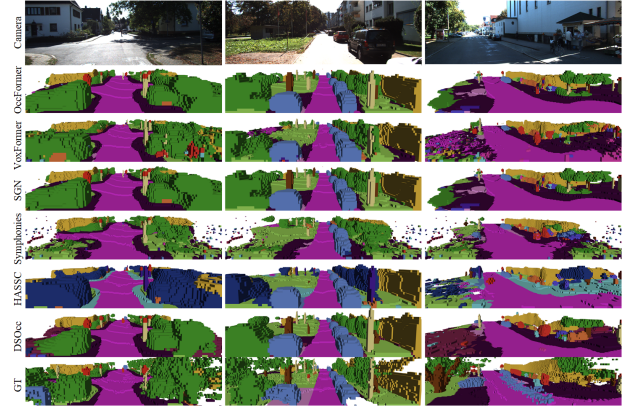


Figure 6: Qualitative comparisons on SemanticKITTI val set.

Qualitative Comparisons. We present the qualitative comparison results on the SemanticKITTI validation set in Fig. 6, with additional examples provided in Appendix C.2. DSOcc can perceive small objects far from the ego vehicle, such as bicyclists and poles, and can clearly distinguish every vehicle in a convoy. In complex scenes, such as corners and shops, DSOcc demonstrates excellent discrimination ability within a local region. This highlights its long-range and class-balanced scene perception, enhancing the reliability and robustness of autonomous driving.

4.4 Ablation Studies

All ablation studies were conducted on the SemanticKITTI val set for DSOcc-T. We focus on four aspects: scene range, input representation, and feature processing. Additional ablation studies are provided in Appendix C.1.

Table 4: Method comparisons in different scene ranges.

Method	25.6m		12.8m	
	IoU	mIoU	IoU	mIoU
VoxFormer-T [27]	57.69	18.42	65.38	21.55
H2GFormer-T [47]	58.51	20.37	67.49	23.43
HASSC-T [46]	58.01	20.27	66.05	24.10
SGN-T [38]	61.90	22.02	70.61	25.70
Ours	61.43	26.48	73.52	31.31

Scene Range. Following the scene range setting in [27, 38, 47, 46], we compare our method using two scene ranges: $25.6m \times 25.6m \times 6.4m$ (25.6m) and $12.8m \times 12.8m \times 6.4m$ (12.8m), as depicted in Table 4. DSOcc maintains state-of-the-art performance in both scene ranges. The scene near the ego vehicle is critical for ensuring the safety of autonomous driving. With a

Table 1: **Quantitative results on SemanticKITTI v1.1.** Bold and underline represent the best and second best results, respectively.

Method	Pub.	IoU	mIoU	Class																		
				car (3.92%)	bicycle (0.03%)	motorcycle (0.03%)	truck (0.16%)	other-veh. (0.20%)	person (0.07%)	bicyclist (0.07%)	motorcyclist (0.05%)	road (15.30%)	parking (1.12%)	sidewalk (1.13%)	other-grnd.(0.56%)	building (14.10%)	fence (3.90%)	vegetation (39.3%)	trunk (0.51%)	terrain (9.17%)	pole (0.29%)	traf.-sign (0.08%)
TPVFormer [16]	CVPR23	35.61	11.36	23.81	0.36	0.05	8.08	4.35	0.51	0.89	0.00	56.50	20.60	25.87	<u>0.85</u>	13.88	5.94	16.92	2.26	30.38	3.14	1.52
OccFormer [54]	CVPR23	36.50	13.46	25.09	0.81	1.19	<u>25.53</u>	8.52	2.78	<u>2.82</u>	0.00	58.85	19.61	26.88	0.31	14.40	5.61	19.63	3.93	32.62	4.26	2.86
VoxFormer-T [27]	CVPR23	44.15	13.35	25.64	1.28	0.56	<u>7.26</u>	7.81	1.93	1.97	0.00	53.57	19.69	26.52	0.42	19.54	7.31	26.10	6.10	33.06	9.15	4.94
PanoSSC [43]	3DV24	34.94	11.22	19.63	0.63	0.36	14.79	6.22	0.87	0.00	0.00	56.36	17.76	26.40	0.88	14.26	5.72	16.69	1.83	28.05	1.94	0.70
H2GFormer-T [47]	AAAI24	44.69	14.29	28.21	0.95	0.91	6.80	9.32	1.15	0.10	0.00	57.00	<u>21.74</u>	29.37	0.34	20.51	7.98	27.44	7.80	36.26	9.88	5.81
OctreeOcc [36]	Arix24	<u>44.71</u>	13.12	28.07	0.64	0.71	16.43	6.03	2.25	2.57	0.00	55.13	18.68	26.74	0.65	18.69	4.01	25.26	4.89	32.47	3.72	2.36
SGN-T [38]	TIP24	46.21	15.32	<u>33.31</u>	0.61	0.46	6.03	<u>9.84</u>	0.47	0.10	0.00	59.10	19.05	29.41	0.33	<u>25.17</u>	<u>9.96</u>	28.93	<u>9.58</u>	38.12	13.25	<u>7.32</u>
Symphonies [19]	CVPR24	41.44	13.44	27.23	<u>1.44</u>	<u>2.28</u>	15.99	9.52	<u>3.19</u>	8.09	0.00	55.78	14.57	26.77	0.19	18.76	6.18	24.50	4.32	28.49	8.99	5.39
HASSC-T [46]	CVPR24	44.55	<u>15.88</u>	30.64	1.20	0.91	23.72	7.77	1.79	2.47	0.00	62.75	20.20	<u>32.40</u>	0.51	22.90	8.67	26.47	7.14	<u>38.10</u>	9.00	5.23
DSOcc-T (Ours)		44.41	18.02	34.08	1.45	7.63	26.60	13.86	5.25	0.56	0.00	<u>60.82</u>	21.76	33.08	0.46	25.30	11.59	<u>28.73</u>	12.21	37.52	<u>12.50</u>	8.87
VoxFormer-S [27]	CVPR23	44.04	12.35	25.79	0.59	0.51	5.63	3.77	1.78	<u>3.32</u>	0.00	54.76	15.50	26.35	<u>0.70</u>	17.65	7.64	24.39	5.08	29.96	7.11	4.18
H2GFormer-S [47]	AAAI24	<u>44.57</u>	13.73	27.60	0.50	0.47	<u>10.00</u>	7.39	1.54	<u>2.88</u>	0.00	56.08	17.83	29.12	0.45	19.74	7.24	26.25	<u>6.80</u>	34.42	7.88	4.68
HASSC-S [46]	CVPR24	44.82	13.48	27.23	0.92	<u>0.86</u>	9.91	5.61	2.80	4.71	0.00	57.05	15.90	28.25	1.04	19.05	6.58	25.48	6.15	<u>32.94</u>	7.68	4.05
SGN-S [38]	TIP24	43.60	<u>14.55</u>	<u>31.88</u>	0.58	0.17	13.18	5.68	1.28	1.49	0.00	<u>59.32</u>	18.46	<u>30.51</u>	0.42	21.43	<u>9.66</u>	<u>25.98</u>	7.43	34.42	9.83	4.71
DSOcc-S (Ours)		42.67	14.59	31.89	<u>0.68</u>	3.67	7.30	<u>6.06</u>	2.40	0.86	0.00	60.30	<u>18.42</u>	31.92	0.53	<u>20.37</u>	11.85	25.53	7.81	32.52	<u>9.68</u>	5.46

Table 2: **Quantitative results on SemanticKITTI hidden test.**

Method	Pub.	IoU	mIoU	Class																		
				car (3.92%)	bicycle (0.03%)	motorcycle (0.03%)	truck (0.16%)	other-veh. (0.20%)	person (0.07%)	bicyclist (0.07%)	motorcyclist (0.05%)	road (15.30%)	parking (1.12%)	sidewalk (1.13%)	other-grnd.(0.56%)	building (14.10%)	fence (3.90%)	vegetation (39.3%)	trunk (0.51%)	terrain (9.17%)	pole (0.29%)	traf.-sign (0.08%)
TPVFormer [16]	CVPR23	34.25	11.26	19.20	1.00	0.50	3.70	2.30	1.10	2.40	0.30	55.10	27.40	27.20	6.50	14.80	11.00	13.90	2.60	20.40	2.90	1.50
OccFormer [54]	CVPR23	34.53	12.32	21.30	1.50	1.70	3.90	3.20	2.20	1.10	0.20	55.90	<u>31.50</u>	30.30	6.50	15.70	11.90	16.80	3.90	21.30	3.80	3.70
VoxFormer-T [27]	CVPR23	43.21	13.41	21.70	1.90	1.60	3.60	4.10	1.60	1.10	0.00	54.10	25.10	26.90	7.30	23.50	13.10	24.40	8.10	24.20	6.60	5.70
SurroundOcc [49]	CVPR23	34.72	11.86	20.30	1.60	1.20	1.40	4.40	1.40	2.00	0.10	56.90	30.20	28.30	6.80	15.20	11.30	14.90	3.40	19.30	3.90	2.40
H2GFormer-T [47]	AAAI24	43.52	14.60	23.70	0.60	1.20	<u>5.20</u>	5.00	1.10	0.10	0.00	57.90	30.00	30.40	6.90	24.00	14.60	25.20	10.70	25.80	7.50	7.10
LowRankOcc [55]	TIP24	45.42	15.76	<u>25.40</u>	4.50	0.90	4.50	3.70	0.50	0.30	0.10	<u>60.40</u>	28.90	31.40	8.70	28.40	18.10	<u>27.40</u>	<u>12.60</u>	28.40	<u>10.00</u>	8.30
Symphonies [19]	CVPR24	38.47	13.56	20.90	3.30	2.70	2.90	4.40	2.40	1.70	2.30	52.80	25.10	27.20	8.80	22.10	14.40	22.90	8.90	20.80	7.00	7.00
Symphonies [19]	CVPR24	42.19	15.04	23.60	<u>3.60</u>	2.60	3.20	<u>5.60</u>	<u>3.20</u>	1.90	<u>2.00</u>	58.40	26.90	29.30	<u>11.70</u>	24.70	16.10	24.20	10.00	23.10	7.70	8.00
HASSC-T [46]	CVPR24	42.87	14.38	23.00	1.90	1.50	2.90	4.90	1.40	<u>3.00</u>	0.00	55.30	25.90	29.60	11.30	23.10	14.30	24.80	9.80	26.50	7.00	7.10
Bi-SSC [50]	CVPR24	45.10	<u>16.73</u>	25.00	1.80	<u>2.90</u>	6.80	6.80	1.70	3.30	1.00	63.40	31.70	33.30	11.20	26.60	19.40	26.10	10.50	<u>28.90</u>	9.30	<u>8.40</u>
DSOcc-T (Ours)		<u>45.12</u>	16.90	25.60	2.50	3.80	4.00	5.20	3.50	0.70	0.00	59.50	29.50	<u>31.80</u>	13.10	<u>27.70</u>	<u>18.20</u>	31.20	13.90	30.30	10.60	9.80
VoxFormer-S [27]	CVPR23	<u>42.95</u>	12.20	20.80	1.00	0.70	<u>3.50</u>	3.70	1.40	2.60	<u>0.20</u>	53.90	21.10	25.30	<u>5.60</u>	19.80	11.10	22.40	7.50	21.30	5.10	4.90
HASSC-S [46]	CVPR24	44.20	13.72	23.40	<u>0.80</u>	<u>0.90</u>	4.80	4.10	1.20	<u>2.50</u>	0.10	56.40	<u>26.50</u>	28.60	4.90	22.80	13.30	<u>24.60</u>	9.10	23.80	6.40	<u>6.30</u>
SGN-S [38]	TIP24	41.88	<u>14.01</u>	24.90	0.40	0.30	2.70	<u>4.00</u>	1.10	<u>2.50</u>	0.30	<u>57.80</u>	27.70	<u>29.20</u>	5.20	<u>23.90</u>	<u>14.20</u>	24.20	10.00	<u>25.80</u>	<u>7.40</u>	4.40
DSOcc-S (Ours)		41.21	14.96	<u>23.70</u>	1.30	1.30	2.70	3.90	<u>1.30</u>	0.90	0.00	60.50	26.20	29.50	12.10	24.00	16.60	26.90	9.30	27.70	7.90	8.40

Table 3: **Quantitative results on SSCBench-KITTI-360 test.**

Method	Pub.	IoU	mIoU	Class																	
				car (2.85%)	bicycle (0.01%)	motorcycle (0.01%)	truck (0.16%)	other-veh. (5.75%)	person (0.02%)	road (14.98%)	parking (2.31%)	sidewalk (6.43%)	other-grnd.(2.05%)	building (15.67%)	fence (0.96%)	vegetation (41.99%)	terrain (7.10%)	pole (0.22%)	traf.-sign (0.06%)	other-struct. (4.33%)	other-obj. (0.28%)
TPVFormer [16]	CVPR23	40.22	13.64	21.56	1.09	1.37	8.06	2.57	2.38	52.99	11.99	31.07	3.78	34.83	4.80	30.08	17.52	7.46	5.86	5.48	2.70
OccFormer [54]	CVPR23	40.27	13.81	22.58	0.66	0.26	9.69	3.82	2.77	54.30	13.44	31.53	3.55	36.42	4.80	31.00	19.51	7.77	8.51	6.95	4.60
VoxFormer-T [27]	CVPR23	38.76	11.91	17.84	1.16	0.89	4.56	2.06	1.63	47.01	9.67	27.21	2.89	31.18	4.97	28.99	14.69	6.51	6.92	3.79	2.43
SGN-T [38]	TIP24	47.06	<u>18.25</u>	<u>29.03</u>	<u>3.43</u>	2.90	10.89	5.20	2.99	58.14	15.04	36.40	4.43	42.02	7.72	<u>38.17</u>	<u>23.22</u>	16.73	16.38	<u>9.93</u>	<u>5.86</u>
Symphonies [19]	CVPR24	44.12	18.58	30.02	1.85	5.90	25.07	12.06	8.20	54.94	13.83	32.76	6.93	35.11	8.58	38.33	11.52	<u>14.01</u>	9.57	14.44	11.28
GaussianFormer [18]	ECCV24	35.38	<u>12.92</u>	18.93	1.02	<u>4.62</u>	<u>18.07</u>	<u>7.59</u>	3.36	45.47	10.89	25.03	<u>5.32</u>	28.44	5.68	29.54	8.62	2.99	2.32	9.51	5.14
DSOcc-T (Ours)		<u>45.12</u>	<u>17.88</u>	27.57	4.23	3.30	13.58	4.66	5.26	<u>57.33</u>	<u>14.40</u>	<u>36.19</u>	3.26	39.86	<u>7.80</u>	36.22	24.28	13.08	<u>16.33</u>	9.52	4.97
DSOcc-S (Ours)		44.88	<u>17.51</u>	27.39	3.05	4.38	13.62	4.82	<u>5.75</u>	57.23	14.38	35.46	2.74	<u>40.85</u>	7.46	35.89	22.90	12.15	15.75	7.71	3.72

31.31 mIoU at the 12.8m range, DSOcc outperforms the second-best method, SGN-T, by 5.61, indicating its ability to make more accurate predictions in proximity to the ego vehicle.

Input Representation. To evaluate the impact of different input representations, we assess four input types: image features in 2D form (Img. 2D), image features in 3D voxel form (Img. 3D), depth, and semantic segmentation map (Sem.). We use the projection-learning module from [27] for the Img. 2D case. As shown in Table 5, Img. 3D improves spatial geometry learning by 0.17 mIoU. Incorporating depth enhances scene completion, yielding a 2.90 IoU gain. We report that depth-aware image feature voxels and semantic-aided voxels achieve 15.00 and 11.16 mIoU, respectively, with standard deviations of 15.09 and 12.76 across all classes. The semantic-aided voxel achieves higher precision on low-proportion classes. For example, the truck class (0.16 %) improves from 3.99 to 10.28. It shows that semantic-aided voxels promote class-balanced predictions.

Table 5: Ablation study for input representation.

Img. 2D	Img. 3D	Depth	Sem.	IoU	mIoU
✓				34.66	10.96
	✓			35.48	11.13 (+0.17)
	✓	✓		38.38	15.00 (+3.87)
		✓	✓	29.50	11.16
	✓	✓	✓	44.41	18.02

Feature Processing. To assess depth embedding methods, we compare the baseline against two variants: depth-concatenation and depth-truncation. They append the depth channel or explicitly set a depth threshold to determine occupancy status. As depicted in Table 6, these methods either increase the burden on feature fusion learning or restrict feature collection, decreasing mIoU by 5.65 and 5.63, respectively. To assess the impact of multi-frame processing in establishing semantic-aided voxel, we compare the baseline with two strategies: using only a single frame (w/t multi. sem.) and concatenating multiple frames (w/t sem. concat.). These approaches either miss potential class information or fail to identify the importance of individual frames.

Table 6: Ablation study for feature processing.

	IoU	mIoU
w/ Depth Trunc.	34.89	12.37 (-5.65)
w/ Depth Concat.	43.31	16.37 (-1.65)
w/o Multi. Sem.	44.65	16.99 (-1.03)
w/ Sem. Concat.	43.24	17.78 (-0.24)
Ours	44.41	18.02

5 Conclusion

In this paper, we propose DSOcc, which leverages depth-aware image feature voxel and semantic-aided voxel to boost 3D semantic occupancy prediction. DSOcc embeds soft occupancy confidence into image features to enable adaptive implicit occupancy state inference, and utilizes image semantic segmentation to aid occupancy class inference, thereby improving robustness. Experimental results demonstrate that DSOcc achieves state-of-the-art performance on the SemanticKITTI dataset among camera-based methods.

References

- [1] Hassan Abu Alhaija, Siva Karthik Mustikovela, Lars Mescheder, Andreas Geiger, and Carsten Rother. Augmented reality meets computer vision: Efficient data generation for urban driving scenes. *Int. J. Comput. Vision*, 126:961–972, 2018.
- [2] Jens Behley, Martin Garbade, Andres Milioto, Jan Quenzel, Sven Behnke, Cyrill Stachniss, and Jurgen Gall. Semantickitti: A dataset for semantic scene understanding of lidar sequences. In *Int. Conf. Comput. Vis.*, pages 9297–9307, 2019.
- [3] Jiawang Bian, Zhichao Li, Naiyan Wang, Huangying Zhan, Chunhua Shen, Ming-Ming Cheng, and Ian Reid. Unsupervised scale-consistent depth and ego-motion learning from monocular video. *Adv. Neural Inform. Process. Syst.*, 32, 2019.
- [4] Holger Caesar, Varun Bankiti, Alex H Lang, Sourabh Vora, Venice Erin Liong, Qiang Xu, Anush Krishnan, Yu Pan, Giancarlo Baldan, and Oscar Beijbom. nuscenes: A multimodal dataset for autonomous driving. In *IEEE Conf. Comput. Vis. Pattern Recog.*, pages 11621–11631, 2020.
- [5] Anh-Quan Cao and Raoul De Charette. Monoscene: Monocular 3d semantic scene completion. In *IEEE Conf. Comput. Vis. Pattern Recog.*, pages 3991–4001, 2022.
- [6] Liang-Chieh Chen, George Papandreou, Iasonas Kokkinos, Kevin Murphy, and Alan L Yuille. Deeplab: Semantic image segmentation with deep convolutional nets, atrous convolution, and fully connected crfs. *IEEE Trans. Pattern Anal. Mach. Intell.*, 40(4):834–848, 2017.
- [7] Xiaozhi Chen, Kaustav Kundu, Ziyu Zhang, Huimin Ma, Sanja Fidler, and Raquel Urtasun. Monocular 3d object detection for autonomous driving. In *IEEE Conf. Comput. Vis. Pattern Recog.*, pages 2147–2156, 2016.
- [8] Marius Cordts, Mohamed Omran, Sebastian Ramos, Timo Rehfeld, Markus Enzweiler, Rodrigo Benenson, Uwe Franke, Stefan Roth, and Bernt Schiele. The cityscapes dataset for semantic urban scene understanding. In *IEEE Conf. Comput. Vis. Pattern Recog.*, pages 3213–3223, 2016.
- [9] Naiyu Fang, Lemiao Qiu, Shuyou Zhang, Zili Wang, Kerui Hu, and Kang Wang. A cross-scale hierarchical transformer with correspondence-augmented attention for inferring bird’s-eye-view semantic segmentation. *IEEE Trans. Intell. Transp. Syst.*, 2024.
- [10] Naiyu Fang, Lemiao Qiu, Shuyou Zhang, Zili Wang, Zheyuan Zhou, and Kerui Hu. Gsd transformer: An efficient and effective cue fusion for monocular multi-frame depth estimation. *IEEE Robotics and Automation Letters*, 9(3):2256–2263, 2024.
- [11] Ziyue Feng, Liang Yang, Longlong Jing, Haiyan Wang, YingLi Tian, and Bing Li. Disentangling object motion and occlusion for unsupervised multi-frame monocular depth. In *Eur. Conf. Comput. Vis.*, pages 228–244, 2022.
- [12] Andreas Geiger, Philip Lenz, Christoph Stiller, and Raquel Urtasun. Vision meets robotics: The kitti dataset. *Int. J. Robot. Res.*, 32(11):1231–1237, 2013.
- [13] Clément Godard, Oisín Mac Aodha, and Gabriel J Brostow. Unsupervised monocular depth estimation with left-right consistency. In *IEEE Conf. Comput. Vis. Pattern Recog.*, pages 270–279, 2017.
- [14] Kaiming He, Xiangyu Zhang, Shaoqing Ren, and Jian Sun. Deep residual learning for image recognition. In *IEEE Conf. Comput. Vis. Pattern Recog.*, pages 770–778, 2016.
- [15] Andrew Howard, Mark Sandler, Grace Chu, Liang-Chieh Chen, Bo Chen, Mingxing Tan, Weijun Wang, Yukun Zhu, Ruoming Pang, Vijay Vasudevan, et al. Searching for mobilenetv3. In *IEEE Conf. Comput. Vis. Pattern Recog.*, pages 1314–1324, 2019.
- [16] Yuanhui Huang, Wenzhao Zheng, Yunpeng Zhang, Jie Zhou, and Jiwen Lu. Tri-perspective view for vision-based 3d semantic occupancy prediction. In *IEEE Conf. Comput. Vis. Pattern Recog.*, pages 9223–9232, 2023.
- [17] Yuanhui Huang, Wenzhao Zheng, Borui Zhang, Jie Zhou, and Jiwen Lu. Selfocc: Self-supervised vision-based 3d occupancy prediction. In *IEEE Conf. Comput. Vis. Pattern Recog.*, pages 19946–19956, 2024.
- [18] Yuanhui Huang, Wenzhao Zheng, Yunpeng Zhang, Jie Zhou, and Jiwen Lu. Gaussianformer: Scene as gaussians for vision-based 3d semantic occupancy prediction. In *Eur. Conf. Comput. Vis.*, pages 376–393, 2025.
- [19] Haoyi Jiang, Tianheng Cheng, Naiyu Gao, Haoyang Zhang, Tianwei Lin, Wenyu Liu, and Xinggang Wang. Symphonize 3d semantic scene completion with contextual instance queries. In *IEEE Conf. Comput. Vis. Pattern Recog.*, pages 20258–20267, 2024.
- [20] Wenjie Lai, Fanyu Zeng, Xiao Hu, Shaowei He, Ziji Liu, and Yadong Jiang. Regseg: An end-to-end network for multimodal rgb-thermal registration and semantic segmentation. *IEEE Trans. Image Process.*, 2024.
- [21] John Lambert, Zhuang Liu, Ozan Sener, James Hays, and Vladlen Koltun. Mseg: A composite dataset for multi-domain semantic segmentation. In *IEEE Conf. Comput. Vis. Pattern Recog.*, pages 2879–2888, 2020.
- [22] Jie Li, Yu Liu, Dong Gong, Qinfeng Shi, Xia Yuan, Chunxia Zhao, and Ian Reid. Rgb-d based dimensional decomposition residual network for 3d semantic scene completion. In *IEEE Conf. Comput. Vis. Pattern Recog.*, pages 7693–7702, 2019.
- [23] Jinke Li, Xiao He, Yang Wen, Yuan Gao, Xiaoqiang Cheng, and Dan Zhang. Panoptic-phnet: Towards real-time and high-precision lidar panoptic segmentation via clustering pseudo heatmap. In *IEEE Conf. Comput. Vis. Pattern Recog.*, pages 11809–11818, 2022.

- [24] Jinke Li, Xiao He, Chonghua Zhou, Xiaoqiang Cheng, Yang Wen, and Dan Zhang. Viewformer: Exploring spatiotemporal modeling for multi-view 3d occupancy perception via view-guided transformers. In *Eur. Conf. Comput. Vis.*, pages 90–106, 2025.
- [25] Rui Li, Dong Gong, Wei Yin, Hao Chen, Yu Zhu, Kaixuan Wang, Xiaozhi Chen, Jinqiu Sun, and Yanning Zhang. Learning to fuse monocular and multi-view cues for multi-frame depth estimation in dynamic scenes. In *IEEE Conf. Comput. Vis. Pattern Recog.*, pages 21539–21548, 2023.
- [26] Yi Li, Haozhi Qi, Jifeng Dai, Xiangyang Ji, and Yichen Wei. Fully convolutional instance-aware semantic segmentation. In *IEEE Conf. Comput. Vis. Pattern Recog.*, pages 2359–2367, 2017.
- [27] Yiming Li, Zhiding Yu, Christopher Choy, Chaowei Xiao, Jose M Alvarez, Sanja Fidler, Chen Feng, and Anima Anandkumar. Voxformer: Sparse voxel transformer for camera-based 3d semantic scene completion. In *IEEE Conf. Comput. Vis. Pattern Recog.*, pages 9087–9098, 2023.
- [28] Yiming Li, Sihang Li, Xinhao Liu, Moonjun Gong, Kenan Li, Nuo Chen, Zijun Wang, Zhiheng Li, Tao Jiang, Fisher Yu, et al. Sscbench: A large-scale 3d semantic scene completion benchmark for autonomous driving. In *IEEE/RSJ Int. Conf. Intell. Robots Syst.*, pages 13333–13340, 2024.
- [29] Yu-Jhe Li, Jinhyung Park, Matthew O’Toole, and Kris Kitani. Modality-agnostic learning for radar-lidar fusion in vehicle detection. In *IEEE Conf. Comput. Vis. Pattern Recog.*, pages 918–927, 2022.
- [30] Zhiqi Li, Wenhao Wang, Hongyang Li, Enze Xie, Chonghao Sima, Tong Lu, Qiao Yu, and Jifeng Dai. Bevformer: learning bird’s-eye-view representation from lidar-camera via spatiotemporal transformers. *IEEE Trans. Pattern Anal. Mach. Intell.*, 2024.
- [31] Xiaodan Liang, Hongfei Zhou, and Eric Xing. Dynamic-structured semantic propagation network. In *IEEE Conf. Comput. Vis. Pattern Recog.*, pages 752–761, 2018.
- [32] Shice Liu, Yu Hu, Yiming Zeng, Qiankun Tang, Beibei Jin, Yinhe Han, and Xiaowei Li. See and think: Disentangling semantic scene completion. *Adv. Neural Inform. Process. Syst.*, 31, 2018.
- [33] Ze Liu, Yutong Lin, Yue Cao, Han Hu, Yixuan Wei, Zheng Zhang, Stephen Lin, and Baining Guo. Swin transformer: Hierarchical vision transformer using shifted windows. In *IEEE Conf. Comput. Vis. Pattern Recog.*, pages 10012–10022, 2021.
- [34] Jonathan Long, Evan Shelhamer, and Trevor Darrell. Fully convolutional networks for semantic segmentation. In *IEEE Conf. Comput. Vis. Pattern Recog.*, pages 3431–3440, 2015.
- [35] I Loshchilov. Decoupled weight decay regularization. In *Int. Conf. Learn. Represent*, page 5, 2019.
- [36] Yuhang Lu, Xinge Zhu, Tai Wang, and Yuexin Ma. Octreeocc: Efficient and multi-granularity occupancy prediction using octree queries. *arXiv preprint arXiv:2312.03774*, 2023.
- [37] Qihang Ma, Xin Tan, Yanyun Qu, Lizhuang Ma, Zhizhong Zhang, and Yuan Xie. Cotr: Compact occupancy transformer for vision-based 3d occupancy prediction. In *IEEE Conf. Comput. Vis. Pattern Recog.*, pages 19936–19945, 2024.
- [38] Jianbiao Mei, Yu Yang, Mengmeng Wang, Junyu Zhu, Jongwon Ra, Yukai Ma, Laijian Li, and Yong Liu. Camera-based 3d semantic scene completion with sparse guidance network. *IEEE Trans. Image Process.*, 2024.
- [39] Mingjie Pan, Jiaming Liu, Renrui Zhang, Peixiang Huang, Xiaoqi Li, Hongwei Xie, Bing Wang, Li Liu, and Shanghang Zhang. Renderocc: Vision-centric 3d occupancy prediction with 2d rendering supervision. In *IEEE Int. Conf. Robot. Autom.*, pages 12404–12411, 2024.
- [40] Jonah Philion and Sanja Fidler. Lift, splat, shoot: Encoding images from arbitrary camera rigs by implicitly unprojecting to 3d. In *Eur. Conf. Comput. Vis.*, pages 194–210, 2020.
- [41] Charles R Qi, Hao Su, Kaichun Mo, and Leonidas J Guibas. Pointnet: Deep learning on point sets for 3d classification and segmentation. In *IEEE Conf. Comput. Vis. Pattern Recog.*, pages 652–660, 2017.
- [42] Faranak Shamsafar, Samuel Woerz, Rafia Rahim, and Andreas Zell. Mobilestereonet: Towards lightweight deep networks for stereo matching. In *IEEE Winter Conf. Appl. Comput. Vis.*, pages 2417–2426, 2022.
- [43] Yining Shi, Jiusi Li, Kun Jiang, Ke Wang, Yunlong Wang, Mengmeng Yang, and Diange Yang. Panossc: Exploring monocular panoptic 3d scene reconstruction for autonomous driving. In *Int. Conf. 3D Vis.*, pages 1219–1228. IEEE, 2024.
- [44] Shuran Song, Fisher Yu, Andy Zeng, Angel X Chang, Manolis Savva, and Thomas Funkhouser. Semantic scene completion from a single depth image. In *IEEE Conf. Comput. Vis. Pattern Recog.*, pages 1746–1754, 2017.
- [45] Xiaoyu Tian, Tao Jiang, Longfei Yun, Yucheng Mao, Huitong Yang, Yue Wang, Yilun Wang, and Hang Zhao. Occ3d: A large-scale 3d occupancy prediction benchmark for autonomous driving. *Adv. Neural Inform. Process. Syst.*, 36:64318–64330, 2023.
- [46] Song Wang, Jiawei Yu, Wentong Li, Wenyu Liu, Xiaolu Liu, Junbo Chen, and Jianke Zhu. Not all voxels are equal: Hardness-aware semantic scene completion with self-distillation. In *IEEE Conf. Comput. Vis. Pattern Recog.*, pages 14792–14801, 2024.
- [47] Yu Wang and Chao Tong. H2gformer: Horizontal-to-global voxel transformer for 3d semantic scene completion. In *AAAI*, pages 5722–5730, 2024.

- [48] Yi Wei, Linqing Zhao, Wenzhao Zheng, Zheng Zhu, Yongming Rao, Guan Huang, Jiwen Lu, and Jie Zhou. Surrounddepth: Entangling surrounding views for self-supervised multi-camera depth estimation. In *Conf. Robot Learn.*, pages 539–549, 2023.
- [49] Yi Wei, Linqing Zhao, Wenzhao Zheng, Zheng Zhu, Jie Zhou, and Jiwen Lu. Surroundocc: Multi-camera 3d occupancy prediction for autonomous driving. In *Int. Conf. Comput. Vis.*, pages 21729–21740, 2023.
- [50] Yujie Xue, Ruihui Li, Fan Wu, Zhuo Tang, Kenli Li, and Mingxing Duan. Bi-ssc: Geometric-semantic bidirectional fusion for camera-based 3d semantic scene completion. In *IEEE Conf. Comput. Vis. Pattern Recog.*, pages 20124–20134, 2024.
- [51] Lihe Yang, Bingyi Kang, Zilong Huang, Xiaogang Xu, Jiashi Feng, and Hengshuang Zhao. Depth anything: Unleashing the power of large-scale unlabeled data. In *IEEE Conf. Comput. Vis. Pattern Recog.*, pages 10371–10381, 2024.
- [52] Zetong Yang, Li Chen, Yanan Sun, and Hongyang Li. Visual point cloud forecasting enables scalable autonomous driving. In *IEEE Conf. Comput. Vis. Pattern Recog.*, pages 14673–14684, 2024.
- [53] Pingping Zhang, Wei Liu, Yinjie Lei, Huchuan Lu, and Xiaoyun Yang. Cascaded context pyramid for full-resolution 3d semantic scene completion. In *Int. Conf. Comput. Vis.*, pages 7801–7810, 2019.
- [54] Yunpeng Zhang, Zheng Zhu, and Dalong Du. Occformer: Dual-path transformer for vision-based 3d semantic occupancy prediction. In *Int. Conf. Comput. Vis.*, pages 9433–9443, 2023.
- [55] Linqing Zhao, Xiuwei Xu, Ziwei Wang, Yunpeng Zhang, Borui Zhang, Wenzhao Zheng, Dalong Du, Jie Zhou, and Jiwen Lu. Lowrankocc: Tensor decomposition and low-rank recovery for vision-based 3d semantic occupancy prediction. In *IEEE Conf. Comput. Vis. Pattern Recog.*, pages 9806–9815, 2024.
- [56] Brady Zhou and Philipp Krähenbühl. Cross-view transformers for real-time map-view semantic segmentation. In *IEEE Conf. Comput. Vis. Pattern Recog.*, pages 13760–13769, 2022.
- [57] Yin Zhou and Oncel Tuzel. Voxelnet: End-to-end learning for point cloud based 3d object detection. In *IEEE Conf. Comput. Vis. Pattern Recog.*, pages 4490–4499, 2018.
- [58] Xizhou Zhu, Weijie Su, Lewei Lu, Bin Li, Xiaogang Wang, and Jifeng Dai. Deformable detr: Deformable transformers for end-to-end object detection. In *Int. Conf. Learn. Represent.*, 2021.

A Occupancy Status Inference for Two-stage Method

We evaluate the Stage-1 module in Voxformer [27] on the SemanticKITTI validation dataset [2]. The occupancy inference results are depicted in Table A1. While the result of FN/N_a appear promising, it is important to note that occupied voxels represent a small proportion of all voxels ($N_v/N_a = 14.60\%$). As a result, 38.14% of occupied voxels are incorrectly inferred as unoccupied. These false negatives do not collect any image features in the subsequent stage, leading to numerous inference errors.

Table A1: The occupancy status inference results for Voxformer. FN , N_a , N_v denote the number of false negative in prediction, the total number of voxels, and the number of occupied voxels in the ground truth, respectively.

Metric	FN/N_a	N_v/N_a	FN/N_v
Value (%)	5.65	14.60	38.14

B The Class Mapping in Image Semantic Segmentation

We use MSeg [21] to predict semantic segmentation maps from camera images, which provides a universal class classification. To align these predictions with the class settings of 3D semantic occupancy prediction, we perform class mapping during the preprocessing step. The class mappings for SemanticKITTI and SSCBench-KITTI-360 [28] are shown in Tables B1 and ??, respectively. This demonstrates that strict alignment in class mapping is not required. Even when some classes are missing in the SemanticKITTI dataset, the semantic-aided voxel still provides sufficient semantic guidance for 3D semantic occupancy prediction.

C Supplementary Experiments

C.1 Supplementary Ablation Study

Image Segmentation Impact. To assess the effect of image segmentation on overall performance, we replaced MSeg [21] with the MobileNet [15] and RegSeg [20] trained on the Cityscapes dataset [8]. As illustrated in Table C1, although these models exhibits lower accuracy and suboptimal class alignment compared to MSeg, it still raises the baseline in mIoU. This improvement confirms the effectiveness of semantic-aided method.

Depth Estimation Error Impact. To assess how depth estimation error affect our model performance, we randomly added noise to the estimated depth to simulate real-world estimation errors. Using the performance

Table B1: The class mapping between SemanticKITTI and MSeg.

SemantiKITTI Label	Class	MSeg Label	Class	SemantiKITTI Label	Class	MSeg Label	Class
0	free			12	other-grnd.	31	road_barrier
1	car	176	car			32	mailbox
2	bicycle	175	bicycle			137	fire_hydrant
3	motorcycle	178	motorcycle			191	wall
				13	building	35	building
4	truck	182	truck	14	fence	144	fence
5	other.-veh.	177	autorickshaw	15	vegetation	131	road_barrier
		180	bus			174	vegetation
		181	train	16	trunk		
		183	trailer	17	terrain	102	terrain
		185	slow_wheeled_object	18	pole	143	pole
6	person	125	person			130	streetlight
7	bicyclist	126	rider_other			145	railing_banister
		127	bicyclist			146	guard_rail
8	motorcyclist	128	motorcyclist			162	column
9	road	98	road	19	traf.-sign.	135	traffic_sign
10	parking	138	parking_meter			136	traffic_light
11	sidewalk	100	sidewalk_pavement				

Table C1: Image segmentation impact.

	mIoU	IoU
Baseline	15.00	8.38
MSeg	18.02	144.41
MobileNet[15]	15.01	42.67
RegSeg[20]	15.13	41.75

of MobileStereoNet [42] on the KITTI 2015 validation set [12] (EPE = 0.79 px) as the baseline, we tested our method across various error ratios. As illustrated in Fig. C1, our method achieves mIoU scores of 16.06 % and 14.96 % when adding one and two times noise, respectively, demonstrating the robustness of soft occupancy confidence.

Depth Using. To assess the advantage of our depth embedding, we compare it against two alternatives: using depth truncation to represent explicit occupancy state and to learn features for occupied voxels [27, 47], and using depth to generate geometric cues that interact with image features [19, 50]. As shown in Table C2, our depth embedding reduces false-negative occupancy predictions and thereby improves mIoU from 13.35 to 15.00. By lifting depth and image features into a spatially aligned 3D representation, our method outperforms the depth-interaction approach, since aligned features enable more accurate fusion.

Table C2: Comparison of depth using.

	mIoU	IoU
Ours	15.00	38.38
In [27, 47]	12.37	34.89
In [19, 50]	14.21	31.71

Soft Occupancy Confidence Calculation. To compare different methods for computing soft occupancy confidence, we evaluated the performance of tanh and sigmoid functions, each combined with a range-mapping operation to normalize inputs from $(0, \infty)$, into $(1, 0)$. As

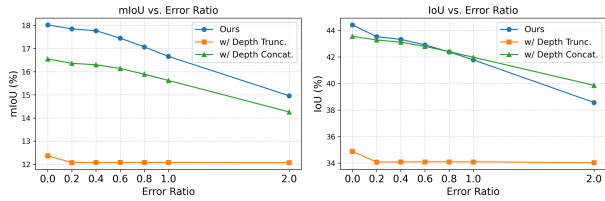


Figure C1: Performance of the method under varying error ratios.

illustrated in Table C3, these functions yield comparable results and effectively meet our objectives. However, our exponential-based function achieved a highest mIoU, indicating its superior performance.

Table C3: Comparison of soft occupancy confidence calculation.

	mIoU	IoU
Ours	18.02	44.41
Tanh	14.85	42.31
Sigmoid	14.99	39.57

Frame Design and Efficiency. To evaluate our frame design and efficiency, especially in the final feature fusion, we introduce a comparison called ‘Three Fus’, which fuses lifted image, segmentation, and depth features via dual interaction. Table C4 reports the inference time of our voxel fusion module alongside other voxel-based learning modules. Our depth-aware fusion attains a higher mIoU than ThreeFus. Our voxel fusion processes dense voxels in 177.07 ms, comparable to the sparse-voxel modules used in VoxFormer [27] and SGN [38].

Table C4: Comparison of fusion mechanisms and efficiency.

	Inf. Time (ms)	mIoU	IoU
Ours	177.07	18.02	44.41
Three Fus	177.07	13.34	34.14
In [27]	84.90	13.35	44.15
In [38]	95.77	15.32	46.21
In [19]	79.03	13.44	41.44

Fusion Mechanism. To evaluate the design of the voxel fusion module, we compare it with five alternatives: using Conv3D layers (Conv.), using Swin Transformer (Swin.), using $\tilde{\mathbf{V}}_t^I$ as the query with DA (Single DA $Q=img.$), using $\tilde{\mathbf{V}}_t^S$ as the query with DA (Single DA $Q=sem.$), and using dual DA with 2 layers (DA 2 layers). As depicted in Table C6, Conv. and Swin. encounter challenges in capturing long-range dependencies, decreasing mIoU by 1.27 and 1.49, respectively. Removing either interaction in baseline also results in mIoU drop. The 2-layer version does not yield any prediction increase but increases inference time to 283.76. In a nutshell, our voxel fusion module strikes a balance between precision and ef-

iciency.

Table C6: Ablation study for fusion mechanism. Inf. Time denotes the inference time of fusion module on per GPUs.

	Inf. Time (ms)	mIoU	IoU
Conv.	0.16	16.75 (-1.27)	40.55
Swin.	0.67	16.53 (-1.49)	41.30
Single DA ($Q=Img.$)	134.52	16.94 (-1.08)	44.69
Single DA ($Q=Sem.$)	134.12	17.88 (-0.14)	42.91
2 Layers DA	283.76	17.48 (-0.54)	45.16
Ours	177.07	18.02	44.41

C.2 Supplementary Qualitative Results

To demonstrate the robustness of DSOcc, we present additional visualization results in Fig. C2. DSOcc effectively identifies each vehicle in front of the ego vehicle. It can also detect small objects, such as pedestrians, cyclists, and poles. Furthermore, DSOcc provides robust scene completion when navigating intersections.

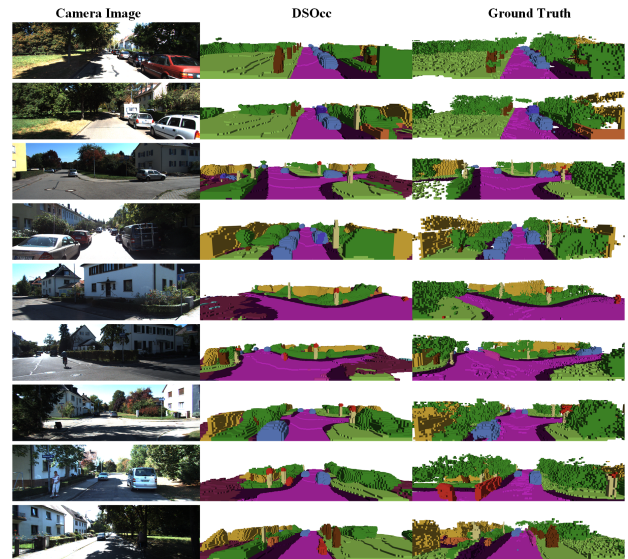


Figure C2: The visualization results of our proposed DSOcc.

C.3 Supplementary Comparison

We also present a quantitative comparison on the Occ3D-nuScenes [45] validation set in Table C5. The dataset comprises 700 training scenes and 150 validation scenes, each annotated within an $80m \times 80m \times 80m$ volume at a voxel resolution $0.4m \times 0.4m \times 0.4m$ for 18 semantic classes. Because Occ3D-nuScenes targets multi-view inputs, unlike our multi-frame setup, we adapt it by disabling multi-segmentation fusion and using only a single frame during DSOcc training. We employ SurroundDepth [48] for

Table C5: Quantitative results on Occ3D-nuScenes validation set. **Bold** and underline represent the best and second best results, respectively.

Method	mIoU	other	barrier	bicycle	bus	car	cons. veh.	motorcycle	pedestrian	traffic cone	trailer	truck	drive. surf.	other flat	sidewalk	terrain	manmade	vegetation
MonoScene [5]	6.06	1.75	7.23	4.26	4.26	4.93	9.38	3.98	3.98	3.90	4.45	7.17	14.91	6.32	7.92	7.43	1.01	7.43
OccFormer [54]	21.93	5.95	21.93	5.85	37.83	17.87	40.44	42.43	7.36	23.88	21.81	20.98	22.38	30.70	55.35	28.36	30.70	18.0
BEVFormer [30]	26.88	5.94	30.29	12.32	34.40	39.17	14.44	16.45	17.22	9.27	13.90	26.36	50.99	30.96	34.66	22.73	6.76	6.97
TPVFormer [16]	27.83	7.22	38.90	13.67	40.78	45.90	17.23	19.99	18.85	14.30	26.69	34.17	55.65	35.47	37.55	30.70	19.40	16.78
CTF-Occ [45]	28.53	8.09	39.33	20.56	38.29	42.24	16.93	24.52	22.72	21.05	22.98	31.11	53.33	33.84	37.98	33.23	20.79	18.00
RenderOcc [39]	26.11	4.84	31.72	10.72	27.67	26.45	13.87	18.2	17.67	17.84	21.19	23.25	63.20	36.42	46.21	44.26	19.58	20.72
Ours	28.40	9.05	32.07	15.22	26.51	39.66	13.65	15.35	17.62	18.40	17.64	22.53	73.73	34.67	42.75	45.68	30.53	27.80

depth estimation and train DSOcc on 8 NVIDIA V100 GPUs. Despite these modifications, DSOcc remains competitive, achieving a mIoU of 20.00

D Limitation

As shown in Fig. C3, when the vehicle rounds a corner, our method sometimes fails to reconstruct the side view because of missing camera features and abrupt changes in vehicle calibration. Our method recognizes this region as the flat other-ground class. This issue could be mitigated by incorporating additional camera viewpoints or by integrating other modalities, such as LiDAR.

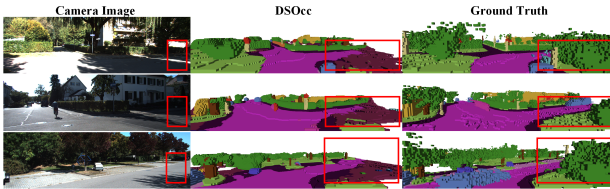


Figure C3: The failure cases.